ELSEVIER

Three-dimensional particle cracking damage development in an Al–Mg-base wrought alloy

A. Balasundaram [a], A.M. Gokhale [a,*], S. Graham [b], M.F. Horstemeyer [b]

[a] *School of Materials Science and Engineering, Georgia Institute of Technology, Atlanta, GA 30332-0245, USA*
[b] *Sandia National Laboratories, Livermore, CA 94551-10969, USA*

Abstract

Experiments have been performed to quantitatively characterize the three-dimensional (3-D) microstructural damage due to cracking of Fe-rich intermetallic particles in an Al–Mg-base extruded 5086(O) alloy as a function of strain under uniaxial compression and tension. The 3-D number density and average volume of the cracked particles are estimated using the unbiased and efficient large area disector (LAD) stereological technique. In each specimen, the two-dimensional (2-D) number fraction of cracked particles is significantly lower than the corresponding 3-D number fraction. Therefore, the conventional 2-D damage measurements considerably underestimate the true 3-D damage due to particle cracking in this alloy. Comparison of the 3-D damage data on the 5086(O) alloy and earlier data on 6061(T6) alloy reveals that at all tensile/compressive stress levels higher than the yield stress of both alloys, the 3-D number fraction of cracked Fe-rich intermetallic particles in the 5086(O) alloy is significantly *lower* than its corresponding value in the 6061(T6) alloy. Therefore, the 5086(O) alloy is less prone to damage progression due to particle cracking compared to the 6061(T6) alloy. In both the alloys, significant rotations of the Fe-rich intermetallic particles occur during deformation under uniaxial compression. These rotations tend to align the particles along the direction of *induced tensile* stretch. The particle rotations in turn affect the progression of damage due to particle cracking. For deformation under uniaxial compression, the average volume of cracked Fe-rich particles *increases* with the increase in the strain. These observations are explained on the basis of the particle rotations.
© 2003 Elsevier Science B.V. All rights reserved.

Keywords: Aluminum alloys; Damage; Microstructure; Ductile fracture; Particle cracking

1. Introduction

Ductile fracture of many industrially important alloys involves cracking of intermetallic inclusions/particles, growth of voids at the cracked particles and void coalescence. Therefore, quantitative characterization and modeling of the damage due to particle cracking are of interest. Microstructural damage, such as particle cracking, is generally of three-dimensional (3-D) nature. Number density and average volume are important geometric attributes of the cracked particles. The particle cracking damage progression can be couched in terms of these microstructural parameters [1–4].

Thus, it is of interest to estimate the number density and average volume of the cracked particles as a function of strain (or number of cycles in the case of cyclic loading) under different loading conditions and stress states.

Microstructures often contain inclusions/particles of different sizes *and* shapes. It is well known that the 3-D topological attributes, such as number density of the cracked particles (or of any other features), *cannot* be estimated from any measurements performed on independent random two-dimensional (2-D) metallographic sections, if all the cracked particles (or any other features of interest) do not have the same geometric shape [5]. Nevertheless, in most of the earlier studies, particle cracking has been quantitatively characterized only in independent random 2-D metallographic planes through the 3-D microstructural space. Therefore,

---

* Corresponding author. Tel.: +1-404-894-2887; fax: +1-404-894-9140.
E-mail address: arun.gokhale@mse.gatech.edu (A.M. Gokhale).

development and applications of general quantitative metallographic techniques for an unbiased and efficient estimation of 3-D microstructural damage are of interest.

Most of the earlier investigations focus on the particle cracking damage evolution under a uniaxial applied tensile stress [6–9]; damage evolution under other test conditions, such as compression and torsion, has received very little attention. Recently, cracking of Fe-rich intermetallic particles has been quantitatively characterized in the 3-D microstructure of an extruded Al–Mg–Si-base precipitation hardened 6061(T6) alloy, which is a typical alloy of 6XXX series. In this alloy, significant differences have been observed in the damage evolution under tension and compression [10,11]. It is of interest to determine if such differences in the path of damage progression exist in other categories of wrought aluminum alloys as well.

5XXX series Al–Mg-base wrought alloys are widely used for structural applications. The ductile fracture of these alloys is also associated with cracking of Fe-rich intermetallic particles. It is the objective of this contribution to quantitatively characterize evolution of 3-D particle cracking damage in an extruded 5086(O) aluminum alloy (which is a typical alloy of 5XXX series) under uniaxial tension and compression and to compare these data with those for 6061(T6) alloy. Note that 5086(O) is a solid solution strengthened alloy that exhibits pronounced dynamic strain aging (DSA), whereas 6061(T6) is a precipitation hardened alloy that does not undergo DSA. It is of interest to study how such differences in the microstructure and deformation characteristics affect the particle cracking damage progression.

In the present study, evolution of the particle cracking damage in an extruded 5086(O) alloy is quantitatively characterized via estimation of 3-D number fraction, volume fraction and average volume of the cracked Fe-rich particles as a function of strain under uniaxial compression and tension using two- and three-dimensional stereological probes and digital image analysis

techniques. Comparison of these data with earlier data on particle cracking in 6061(T6) alloy reveals that 5086(O) alloy is significantly less prone to the particle cracking damage compared to 6061(T6) alloy. The differences in the particle cracking damage progression in the two alloys are explained on the basis of the differences in their microstructure and deformation characteristics.

2. Experimental

2.1. Materials and mechanical tests

The experiments were performed on commercial 5086(O, annealed) aluminum alloy specimens from an extruded round bar of 44 mm diameter. The chemical composition of the bar stock, as revealed by a spectrochemical analysis performed by FTI Anamet Corp., is given in Table 1. All specimens were extracted from the bar stock using wire EDM at a radial distance of 10 mm from the bar center. This was carried out to ensure that different specimens have statistically similar initial microstructures. The damage was characterized in the specimens subjected to different strain levels under uniaxial tension and compression. All tests were performed with the loading direction parallel to the extrusion axis.

The compression test specimens were designed to induce a predominantly compressive stress state. These specimens were in the form of cylinders of 9 mm diameter and 12.5 mm length. Concentric grooves were machined into the ends of the specimens and filled with a molybdenum disulfide lubricant (Molykote G-N paste supplied by Dow Corning). The lubrication was necessary to ensure homogeneous deformation of the specimens. Quasi-static interrupted uniaxial compression tests were performed on an MTS81-axial-torsional servo-hydraulic test frame at a strain rate of 2×10^{-4} s^{-1}. The loads and the specimen displacements were measured using a resident load cell, LVDT and RVDT. The specimens were examined at the end of each test; no barreling effects were seen. Thus, homogeneous deformation conditions can be assumed for the compression tests. Fig. 1 shows a typical stress–strain curve obtained in this manner. Observe that there is a serrated flow beyond a critical strain, indicating the presence of dynamic strain aging [12].

The tensile test specimens were in the form of cylinders of 6 mm diameter and 60 mm length having smooth sidewalls to induce uniform tensile stress states up to the point of instability. Interrupted uniaxial tensile tests were performed on an MTS 880 servo-hydraulic test frame in a displacement controlled mode at a displacement rate of 5×10^{-3} mm s^{-1}. The load was measured using a resident load cell and the strain was

Table 1
Composition of 5086 alloy

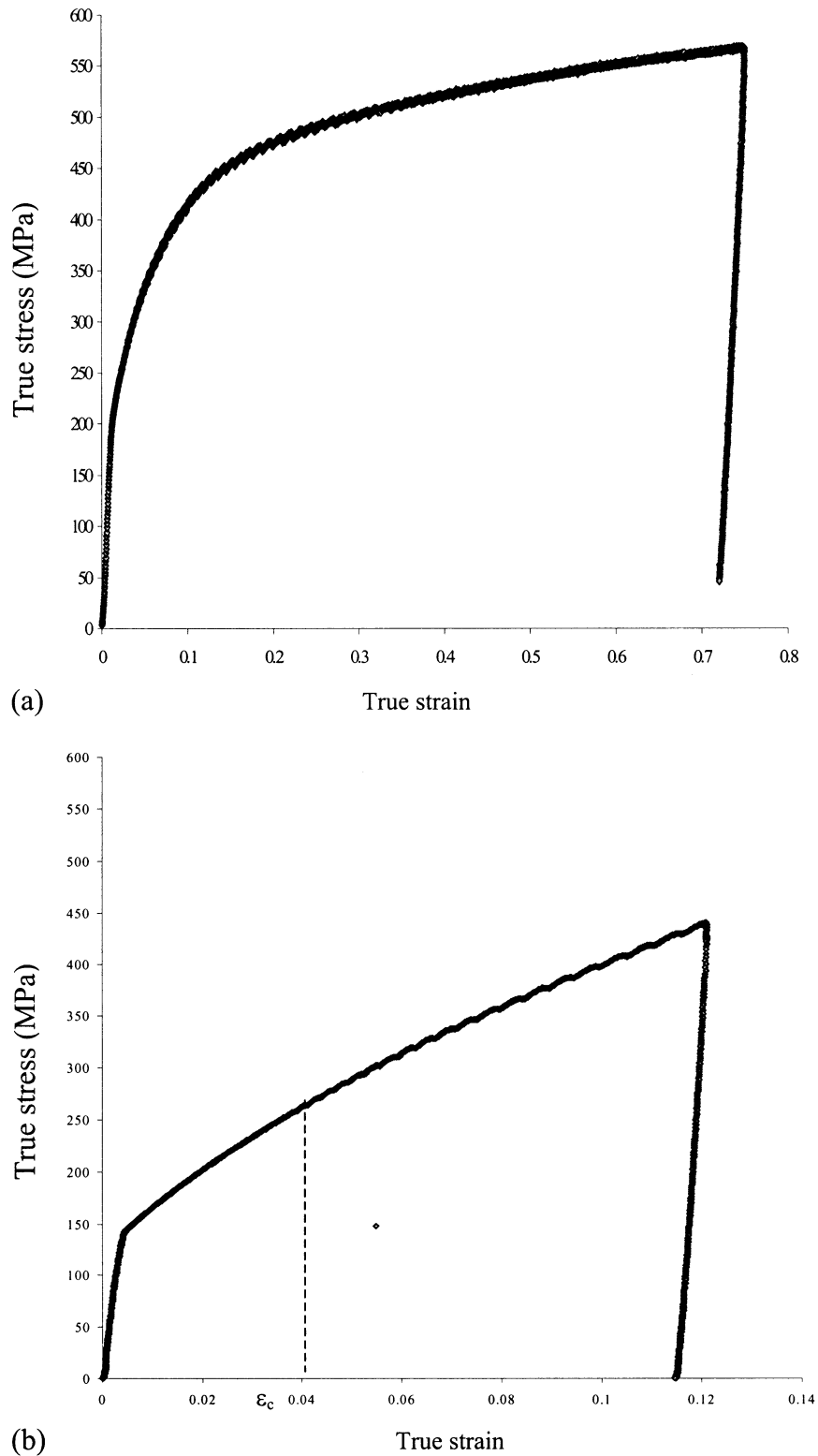| Element	wt.%
Cr	0.11
Mg	3.95
Si	0.12
Mn	0.56
Fe	0.18
Cu	0.06
Ti	0.03
Zn	0.07
Other	0.05
Al	Balance

Fig. 1. True stress–true strain curve for 5086(O) Al-alloy specimen under compressive loading (a) up to 0.75 strain and (b) up to 0.13 strain.

measured with two clip-on extensometers. Fig. 2 shows a typical stress–strain curve of a specimen in tension. Observe that there is highly serrated flow beyond a critical strain of ≈ 0.08, indicating the presence of dynamic strain aging.

2.2. Metallography

The specimens were cut in the center along a vertical plane containing the loading direction (which is also the direction of the extrusion axis) and then mounted in a
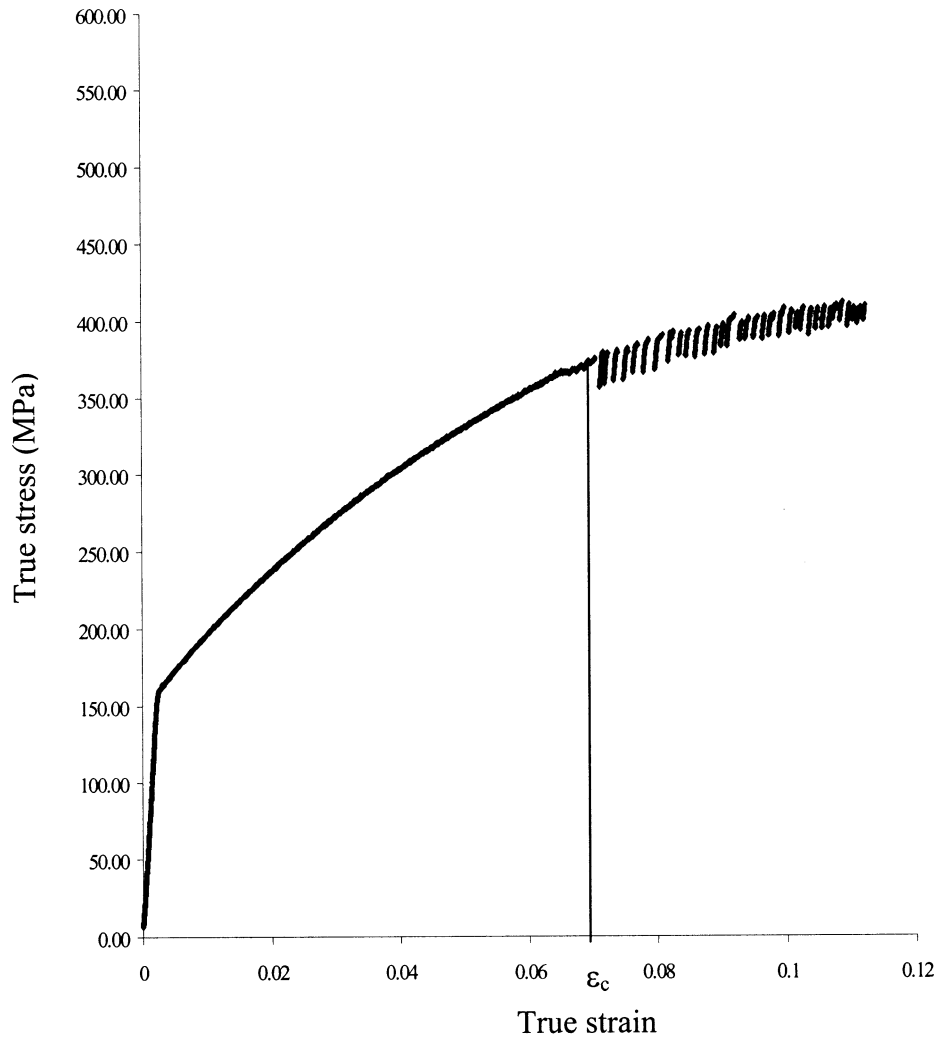
Fig. 2. True stress–true strain curve of 5086(O) Al-alloy specimens in tension.

polymer mount. These samples were polished using standard metallographic techniques. Final polishing was a two-step process: the first step consisting of polishing with 0.05-micron alumina solution and the second step involving polishing with 100% colloidal silica solution on a microcloth. The specimens were then rinsed with methanol, dried and observed under a light microscope in the unetched condition. Fig. 3 shows a typical microstructure of an unstrained specimen in unetched condition. Observe that the microstructure contains two types of particles in the aluminum-rich matrix: the light gray particles are the Fe-rich intermetallic particles (Fe, Mn) Al_6, whereas the dark particles are Mg base intermetallics (Mg_2Si or Al–Fe–Cr–Si with some Mg) [14]. Note that both types of particles are clustered in bands oriented parallel to the extrusion axis, which is also the loading direction for all specimens. Further, the particles have anisotropic or-

ientations: most of the particles have their major axes parallel (or almost parallel) to the extrusion axis. For comparison, a typical microstructure of an unstrained specimen of 6061(T6) alloy in an unetched condition is shown in Fig. 4. Inspection of Figs. 3 and 4 reveals significant similarities in the morphology of the Fe-rich intermetallic particles in the two alloys. However, the chemical composition of the constituent particles in 6061(T6) alloy is different from those in the 5086(O) alloy. The light gray particles in the 5086(O) alloy are of type (Fe, Mn) Al_6, whereas those in the 6061(T6) alloy are of type (($Fe,Mn,Cr)_3SiAl_{12}$,$(Fe,Mn,Cr)_2Si_2Al_9$). Further, the dark particles in 5086(O) alloy are of the type Mg_2Si or Al–Fe–Cr–Si with some Mg, whereas those in the 6061(T6) alloy are of the Mg_2Si. In addition, there are differences in the volume fraction, average size and shape of the Fe-rich intermetallic particles in the two alloys. These differences in the chemistry and
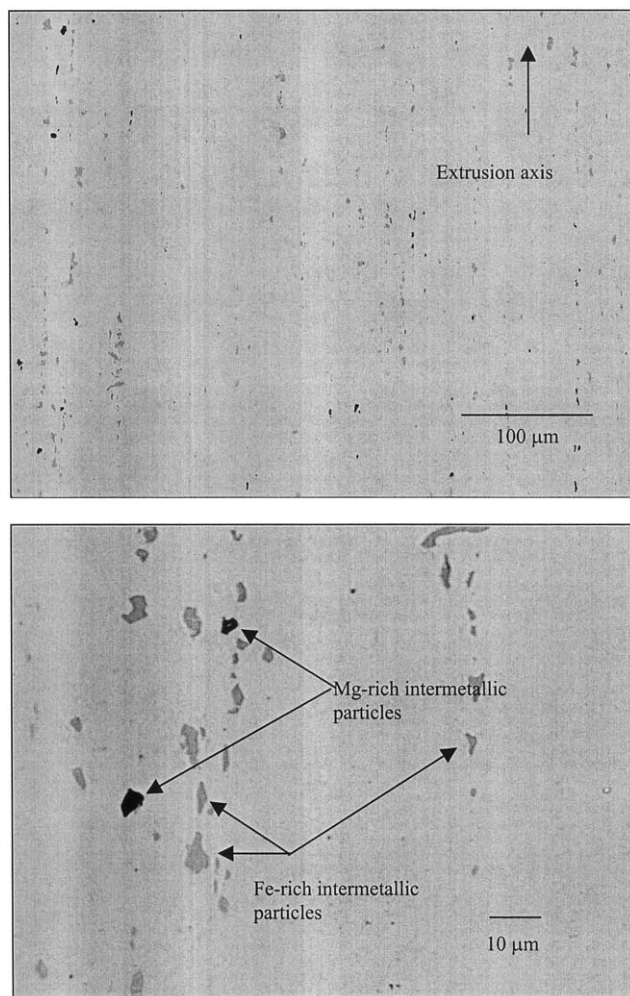
Fig. 3. Microstructure of an unstrained specimen of 5086(O) alloy in unetched condition: (a) microstructural montage of 100 contiguous fields and (b) one field of view from the montage in (a) shown at the resolution level at which the montage was created.
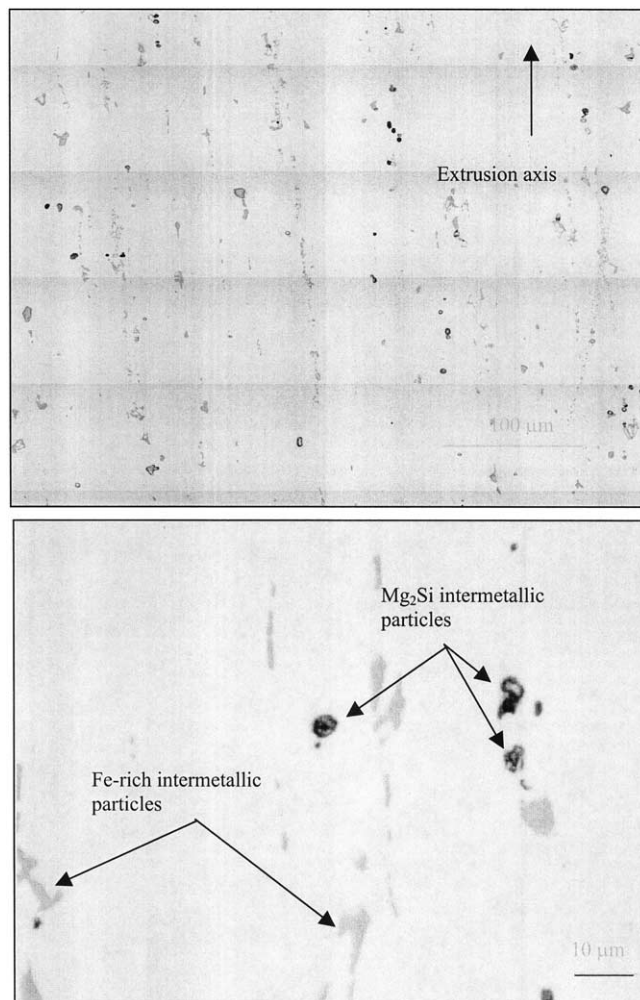

Fig. 4. Microstructure of an unstrained specimen of 6061(T6) alloy in unetched condition: (a) microstructural montage of 100 contiguous fields and (b) one field of view from the montage in (a) shown at the resolution level at which the montage was created.

geometry of the Fe-rich intermetallic particles partly account for the observed differences in the particle cracking damage accumulation in the two alloys.

Figs. 5 and 6 depict microstructures of strained 5086(O) aluminum alloy specimens showing cracked Fe-rich intermetallic particles. In the 5086(O) alloy (as well as in 6061(T6) alloy [10,11]), the damage due to cracking of Mg-based intermetallics (dark particles) is observed to be negligible in comparison to that due to cracking of Fe-based intermetallics. Therefore, in the present study, cracking of only the Fe-rich intermetallics has been quantitatively characterized. The cracked Fe-rich particles are detected via the contrast resulting from the separation of the conjugate crack traces observed in the cracked particles. It follows that only those cracks (and therefore, the cracked particles) having crack separation larger than the resolution limit of the optical microscope (≈ 0.3 microns) can be detected in this manner.

2.3. Quantitative metallography

Digital image analysis and stereological techniques were used to quantify the 3-D number fraction, volume fraction and average volume of cracked Fe-rich particles at different compressive and tensile strain levels. In each specimen, the measurements have been performed on $\approx$ 600 microstructural fields (≈ 5 mm^2 area). The volume fraction of cracked Fe-rich particles was estimated using standard stereological techniques [5]. The 3-D number density of particles, i.e. number of particles per unit volume of microstructure, can be estimated in two ways: (1) by reconstructing the three-dimensional microstructural volume from a stack two-dimensional serial sections and counting the number of particle centroids in the reconstructed microstructural volume segment; or (2) by unbiased counting of particles in the three-dimensional microstructural space using a pair of planes at random locations and following either disector [15],
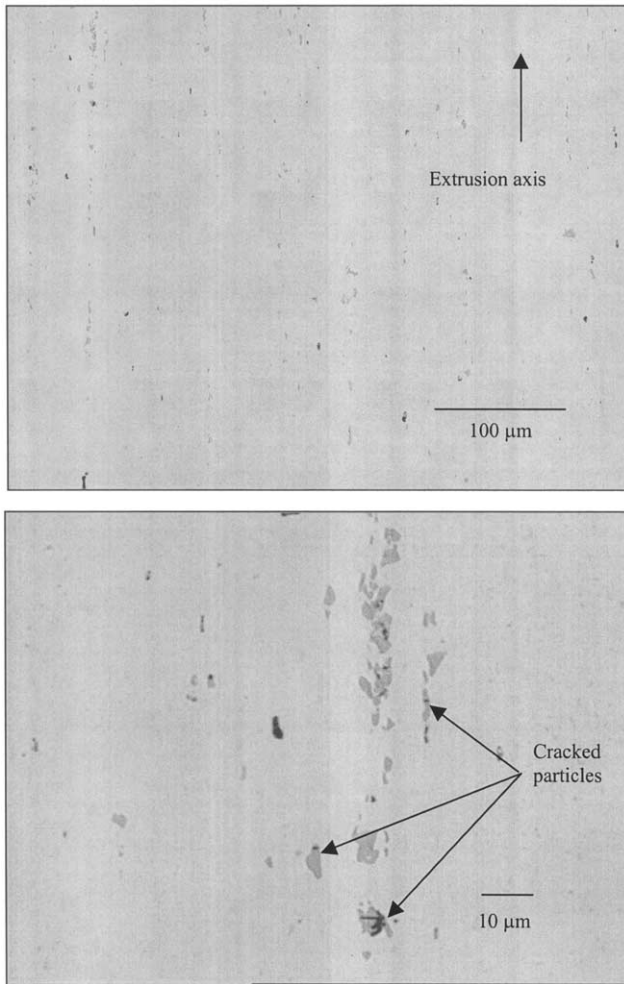
Fig. 5. Microstructure of fractured tensile test specimen (0.12 strain) of 5086(O) alloy: (a) microstructural montage of 100 contiguous fields and (b) one field of view from the montage in (a) shown at the resolution level at which the montage was created. Observe that the particle cracks are mostly *perpendicular* to the extrusion axis, which is also the loading direction.
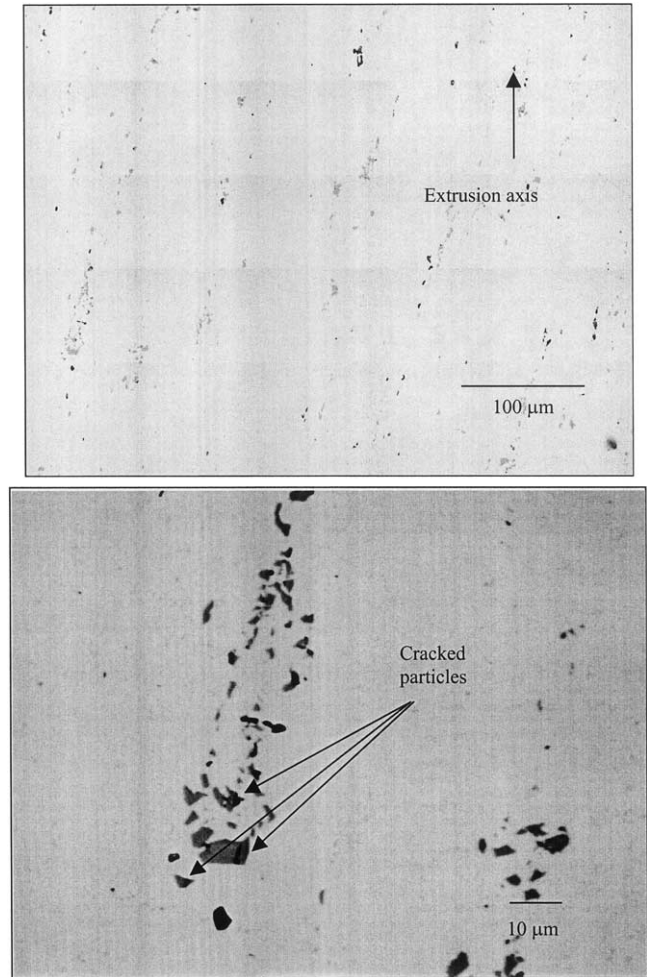

Fig. 6. Microstructure of fractured compression test specimen (0.75 strain) of 5086(O) alloy: (a) microstructural montage of 100 contiguous fields and (b) one field of view from the montage in (a) shown at the resolution level at which the montage was created. Observe that the particle cracks are mostly *parallel* to the extrusion axis, which is also the loading direction.

or large area disector [16,17] methodology. The first approach is laborious and inefficient. The second approach (particularly the one based on large area disector) is general, efficient and unbiased. Disector is a stereological sampling probe that consists of a set of two parallel planes that are a small distance apart [15]. The particles that appear in the first plane but are not present in the second plane of the disector are counted (let this number be Q^-). Similarly, the particles that are not present in first plane, but are present in the second of the disector, are also counted (let this number be Q^+). The unbiased estimate of the number of these features per unit volume, N_V, is given by the following general unbiased stereological relationship [15]:

$$N_V = [Q^+ + Q^-]/[2.A.h] \qquad (1)$$

In the above equation h is the distance between the two planes of the disector probe and A is the area of the disector. This technique makes no assumptions about the shape, size or distribution of the features of interest.

In the present study, large area disector (LAD) methodology has been adopted, as it is efficient as well as unbiased [16,17]. In this methodology, a *montage* of a large number of contiguous two-dimensional microstructural fields is grabbed in the first metallographic plane using image analysis techniques [13]. The specimen is then polished to remove a small thickness (in the present case, 1 μm) of the material. A two-dimensional montage of the same number of microstructural fields is then grabbed on the second metallographic plane exactly at the same (x, y) position as the first one. In the present work, the LAD planes were aligned by using

the locations of micro-hardness indents for reference. The thickness of material removed (i.e. distance between the LAD planes, h) was calculated by measuring the difference in the diagonal length of the diamond indents in the two LAD planes, which is related to the material thickness removed h through the geometry of the micro-hardness indentor. From the experimental measurements of Q^+, Q^- and h, the number of particles per unit volume can be estimated using Eq. (1). For representative statistical sampling, in the present study, three sets of LADs were analyzed to estimate the average 3-D number density of the cracked Fe-rich intermetallic particles in each specimen. A similar procedure was also used to estimate the number density of overall population of the Fe-rich intermetallic particles (cracked as well as undamaged). From these experimental data, the 3-D *number fraction* of the cracked Fe-rich particles, F, was estimated in each specimen. For comparison, the 2-D number fraction of cracked Fe-rich particles in metallographic planes, f, was also measured in each specimen. Further, from the experimental data on the number density of the cracked particles, N_V and their volume fraction, V_V, the average volume of cracked and bulk Fe-rich intermetallic particles was calculated by using the following relationship:

$$\bar{V} = \frac{V_V}{N_V} \tag{2}$$

3. Results and discussion

3.1. Mechanical behavior of 5086 Al-alloy

Fig. 1 shows the true stress–true strain curve of the 5086(O) alloy under uniaxial compression. Observe that there is a serrated plastic flow beyond a critical strain, indicating the presence of dynamic strain aging (DSA). The critical strain for onset of DSA is ≈ 0.04 for deformation under uniaxial compression. Fig. 2 shows the true stress–true strain curve of the 5086(O) Al-alloy under uniaxial tension. Notice again, that there is a highly serrated flow after a critical strain of ≈ 0.08, indicating the presence of dynamic strain aging under tensile loading as well. For comparison, the true stress–true strain curves for 6061(T6) alloy in tension and compression [1011] are shown in Figs. 7 and 8, respectively. Inspection of these stress–strain curves reveals the following:

1) Dynamic strain aging is observed in the 5086(O) alloy in both tension and compression, whereas it is not observed in the 6061(T6) alloy.

2) The 5086(O) alloy has lower yield stress and a higher strain-hardening coefficient than the 6061(T6) alloy.

As mentioned earlier, 5086(O) is a solid solution strengthened alloy, whereas 6061(T6) is a precipitation-hardened alloy. Although both alloys contain Mg, 5086(O) alloy has a significantly higher amount of Mg (3.5–4.5)% than 6061(T6) alloy (0.8–1.2)%. The Si content is, however, higher in the 6061(T6) alloy (0.4–0.8)% compared to the 5086(O) alloy (0.4% max). Therefore, in the 6061(T6) alloy, most of the Mg is locked up in Mg_2Si precipitates and Mg-rich constituent particles and, consequently, sufficient Mg atoms are not available to form the solute atmospheres around the dislocations that can lead to DSA [18–22]. Due to this reason, DSA is not observed in the 6061(T6) alloy. On the other hand, in the 5086(O) alloy, due to the lower amount of Si, an insufficient amount of Mg_2Si precipitates is formed and, therefore, there is no precipitation hardening, but as most of the Mg is in solid solution, pronounced DSA is observed. The higher yield stress of 6061(T6) alloy is primarily due to precipitation hardening, whereas the higher strain-hardening coefficient of 5086(O) alloy is essentially due to the presence of DSA [23]. These differences in the deformation characteristics are partly responsible for the observed differences in the particle cracking damage progression in these alloys.

3.2. Bulk microstructure of 5086(O) and 6061(T6) alloys

The quantitative microstructural data for the unstrained 5086(O) Al-alloy specimens are given in Table 2. For comparison, the corresponding data on unstrained 6061(T6) alloy obtained in the earlier study [10] are also given in Table 2. The volume fraction, number density, aspect ratio and average volume of Fe-rich intermetallic particles are higher in the 6061(T6) alloy compared to those in the 5086(O) alloy. It is well known that the larger and elongated particles (high aspect ratio) crack at lower stresses. Therefore, higher particle cracking damage observed in the 6061(T6) alloy compared to that in the 5086(O) alloy is partly due to the differences in the amount, size, shape and number density of the Fe-rich particles in the two alloys.

3.3. Qualitative microstructural observations on particle cracking

Figs. 5 and 6 depict unetched microstructures of the specimens deformed in tension and compression, respectively. Inspection of the microstructures of these and other specimens lead to the following observations.
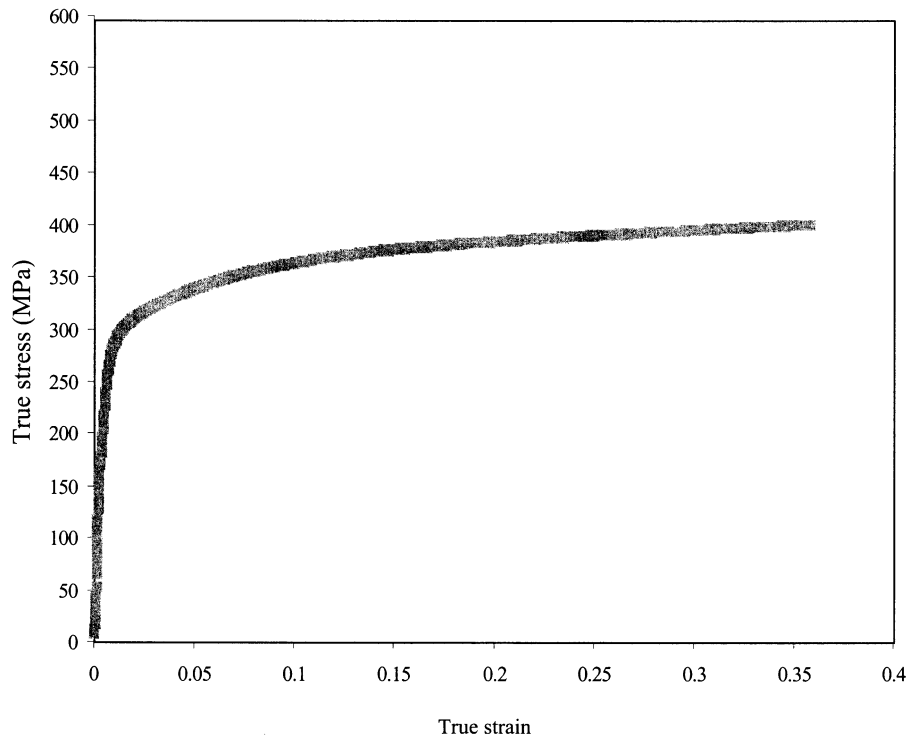
Fig. 7. True stress–true strain curve for 6061(T6) Al-alloy specimen under compressive loading.

1) In the tensile test specimens, the cracks in the damaged particles are mostly *perpendicular* to the loading direction, whereas those in the compression test specimens are mostly *parallel* to the loading direction. Therefore, the anisotropy of the crack orientations strongly depends on the loading condition and stress state.

2) The cracks are mostly *perpendicular* to the direction of the major axis of the corresponding Fe-rich intermetallic particles in both tensile and compression test specimens. Therefore, particle cracking is strongly influenced by the local maximum principal stretch.

3) There are no debonded particles in both tensile and compression test specimens. Therefore, particle cracking is the dominant damage nucleation mode in tension as well as compression.

The above observations are essentially the same as those on the cracked Fe-rich intermetallic particles in the 6061(T6) Al-alloy [10,11]. Therefore, *qualitatively,* the Fe-rich particle cracking damage in the 5086(O) Al-alloy is similar to that observed in the 6061(T6) alloy. However, as shown in the subsequent sections, there are significant differences in the *quantitative* data on the particle cracking damage evolution in the two alloys.

3.4. Particle cracking under uniaxial compression

Fig. 9 shows variation of the average cracked particle volume with compressive strain in the 5086(O) and 6061(T6) alloys. Observe that, in both alloys, the average volume of the cracked particles *increases* with increase in compressive strain in a monotonic manner. In the 5086(O) alloy, the average volume of cracked particles at the highest compressive strain level studied (0.75 strain) is larger than that at the lowest strain studied (0.125) by almost a factor of three. A similar trend has been observed for the strain dependence of average volume of cracked particles in the 6061(T6) alloy as well, and a similar explanation [10,11] can also be given for the present experimental data. An increase in average cracked particle volume with strain implies that more and more *larger* particles crack at progressively higher compressive strain/stress levels. Gurland and Plateau [9] have given following equation for critical tensile stress σ to develop a crack in a particle of size D.

$$\sigma = [E\gamma/(Dq^2)]^{1/2} \tag{3}$$

In Eq. (3), q is the stress concentration factor at the particle, E is weighted average of the elastic moduli of the particle and matrix and γ is the interfacial energy of the crack. Thus, the stress σ required to crack a particle is inversely proportional to the square root of the
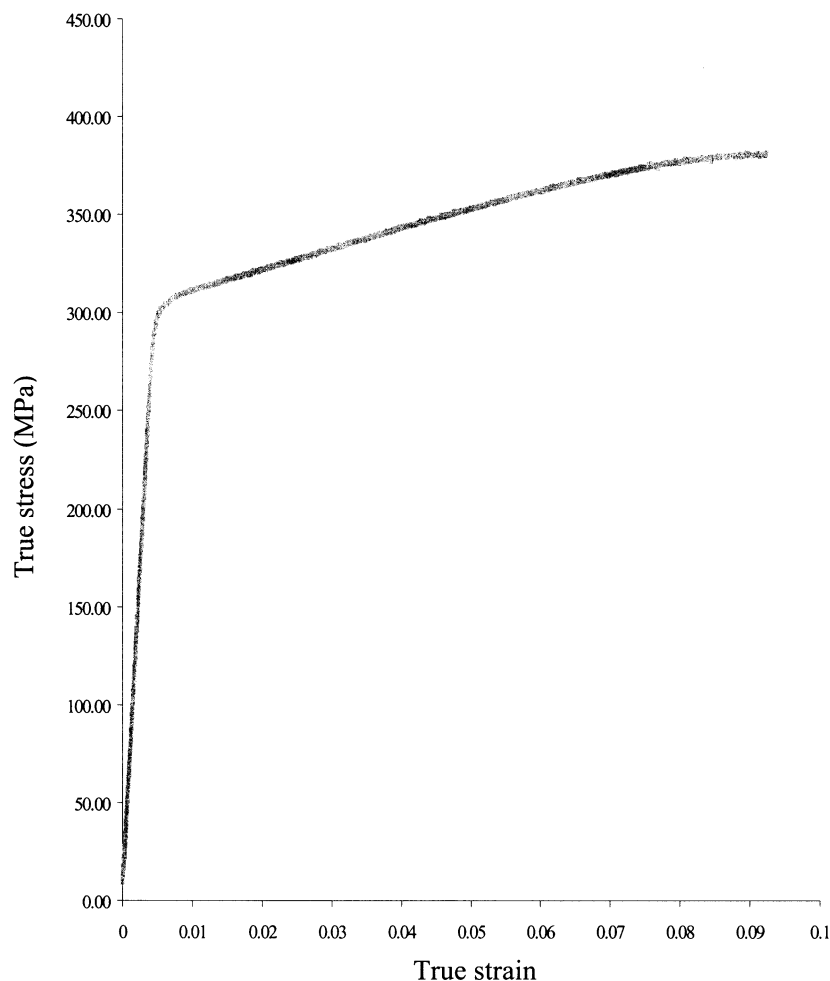
Fig. 8. True stress–true strain curve for 6061(T6) Al-alloy specimens in tension.

Table 2
Microstructural attributes of Fe-rich intermetallic particles in unstrained 5086(O) and 6061(T6) alloy specimens

Microstructural parameter	5086(O) alloy	6061(T6) alloy
Volume fraction (%)	0.76	1.0
Average particle volume $(\mu m)^3$	72	91
Average aspect ratio	1.9	2.08
Average number density number per $(\mu m)^3$	1.05×10^{-4}	1.1×10^{-4}

particle size and, accordingly, larger particles crack at lower stresses. Therefore, as damage accumulates, the largest particles are expected to fracture at the lowest stress levels and progressively smaller particles may crack at higher and higher stress levels. As a result of such damage progression, the average volume of cracked particles is expected to *decrease* with increase in strain, which is *opposite* to what is observed experimentally in the present investigation. Therefore, the observed increase in average cracked particle volume with compressive stress (or strain) cannot be explained

on the basis of existing particle-cracking theories. However, it must be recognized that all particle-cracking theories implicitly assume that the brittle inclusions/ particles remain *stationary* as the ductile matrix undergoes plastic deformation. However, if the brittle Fe-rich particles *rotate* as the ductile aluminum-rich matrix deforms, then the particle rotations can bring new Fe-rich particles into morphological orientations that may facilitate particle cracking, which can then affect the damage progression. Thus, it is of interest to determine if significant rotations of Fe-rich intermetallic particles occur during the deformation of 5086(O) alloy when a compressive stress is applied parallel to the extrusion axis.

The orientation of a particle can be specified by the angle θ between the major axis of the particle and the loading direction (which is the extrusion axis). The orientation angles of the Fe-rich particles can be measured in the metallographic plane using image analysis and the morphological orientation distribution can be computed from such data. Significant changes in the morphological orientation distribution function with
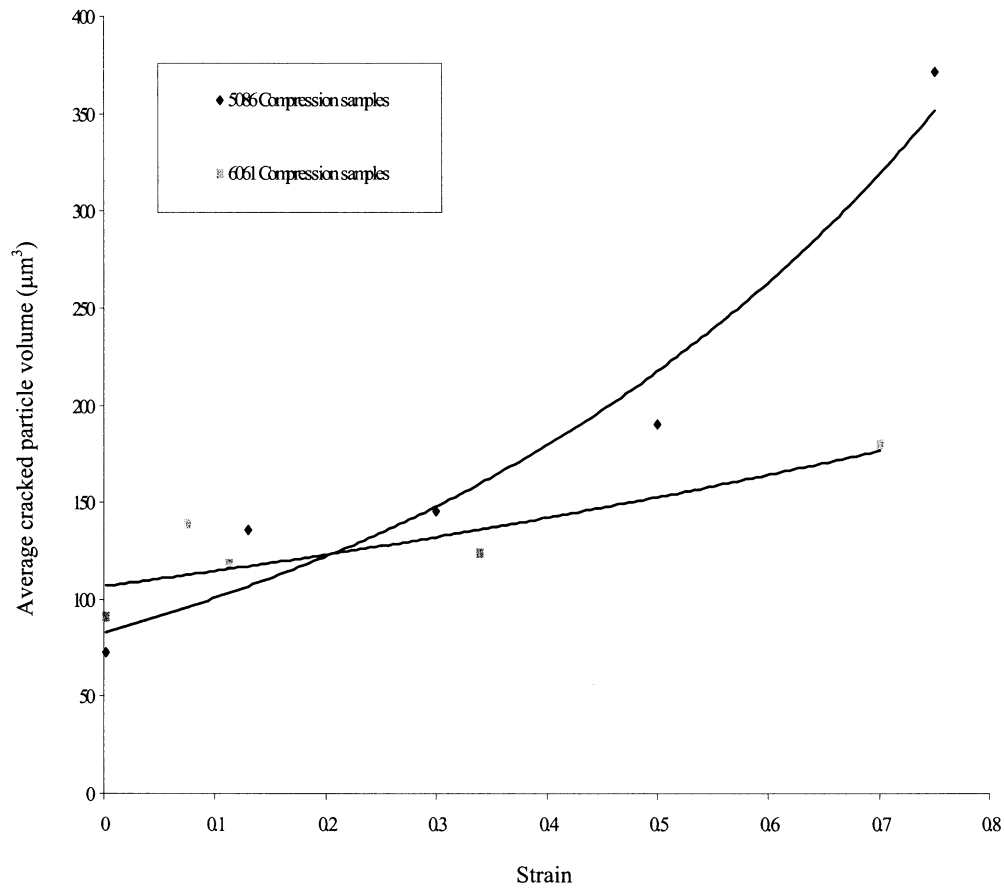
Fig. 9. Plot of average volume of cracked Fe-rich particles in 5086(O) and 6061(T6) alloys versus compressive strain.
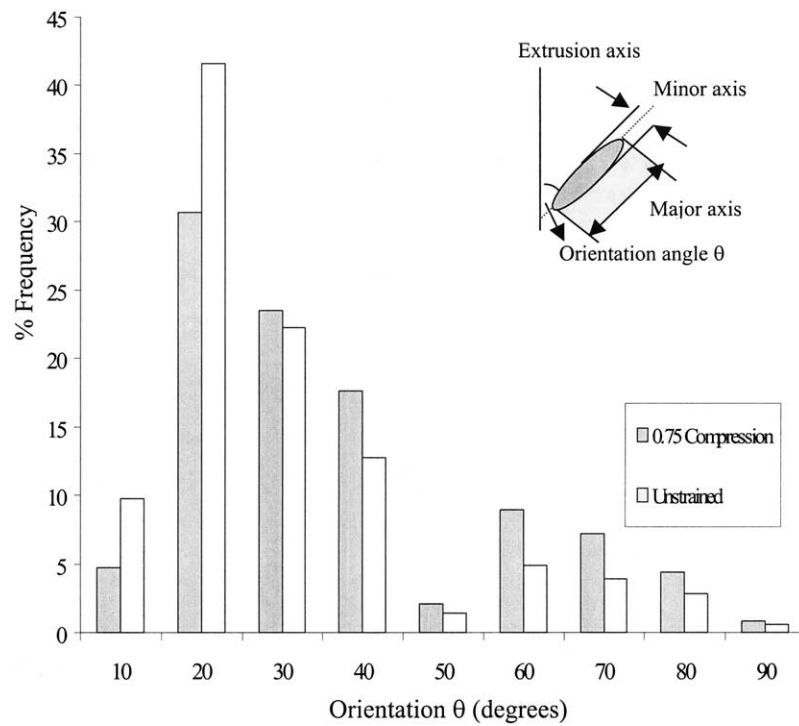

Fig. 10. Comparison of the morphological orientation distribution of Fe-rich intermetallic particles in the unstrained specimen of 5086(O) alloy with the corresponding distribution in the specimen with 0.75 compressive strain.

the strain are then indicative of the particle rotations. Fig. 10 compares the experimentally measured morphological orientation distribution of the Fe-rich intermetallic particles in the unstrained specimen of the alloy with that in the specimen strained to 0.75 strain in compression. These data include both undamaged and damaged particles. In the unstrained specimen, $\approx 70\%$ of the particles have orientations in the range of $0-30°$ and $\approx 10\%$ are oriented in the range of $60-90°$. Therefore, most of the particles tend to align themselves along the extrusion axis, which is quite expected in the microstructure of an extruded alloy. In the 0.75 compressive strained specimen, $\approx 60\%$ of the particles have orientations in the range of $0-30°$, whereas $\approx 20\%$ of the particles have orientations in the range of $60-90°$. Therefore, 0.75 deformation under uniaxial compression parallel to the extrusion axis leads to an increase in the percentage of particles in the orientation range of $60-90°$ from 10 to 20% (i.e. % is doubled) and it decreases the percentage of particles in the orientation range of $0-30°$ from 70 to 60%. Clearly, under uniaxial compression along the extrusion axis, the Fe-rich particles rotate and tend to align themselves along the direction *perpendicular* to the loading direction, which is the direction of *induced tensile stress*. It is well known that the particles aligned parallel (or almost parallel) to the induced (or applied) tensile stress have a higher probability of cracking compared to the particles of the same size and shape oriented perpendicular to the induced (or applied) tensile stress. Therefore, the particle rotations bring *new* large particles in the orientations almost parallel to the induced tensile stress, which facilitates the cracking of additional large particles. Such damage progression should lead to an increase in the average volume of cracked particles with an increase in compressive strain, as observed experimentally. Thus, the present data clearly demonstrate that there is a strong link between the particle rotations and particle cracking damage evolution in 5086(O) alloy. Extensive experimental data on particle rotations in the 5086(O) alloy are presented elsewhere [23,24].

Significant rotations of Fe-rich intermetallic particles also occur in the extruded 6061(T6) alloy, when a compressive load is applied parallel to the extrusion axis [10,22]: a plastic deformation of 0.70 strain leads to an increase in the percentage of particles in the orientation range of $60-90°$ from 7% (in the initial microstructure) to 30% (i.e. increase of a factor of four) and it decreases the percentage of particles in the orientation range of $0-30°$ from 77 to 43%. On the other hand, in the 5086(O) alloy, a comparable deformation under compression (0.75 strain) leads to an increase in the percentage of particles in the orientation range of $60-90°$ from 10 to 20% (i.e. % is doubled) and it decreases the percentage of particles in the orientation range of $0-30°$ from 70 to 60%. Therefore, although the particle

rotation occurs in both the alloys, the extent of particle rotation is significantly less in the 5086(O) alloy compared to that in the 6061(T6) alloy under a compressive loading applied parallel to the extrusion axis. The lower tendency of particle rotation in the 5086(O) alloy partly accounts for the observed lower particle cracking damage in this alloy compared to the 6061(T6) alloy.

Fig. 9 compares the variation of average cracked particle volume of Fe-rich particles with compressive strain in the 5086(O) and 6061(T6) microstructures. Observe that, in the 6061(T6) alloy, at the highest compressive strain level studied (70%), the average cracked particle volume is lower by almost a factor of two than that at the comparable strain level (75%) in the 5086(O) alloy. Further, the rate of increase of average cracked particle volume is also significantly higher in the 5086(O) alloy compared to that in 6061(T6) Al-alloy under compression. Therefore, with an increase in the applied compressive stress, more *larger* particles crack in the 5086(O) alloy compared to those in the 6061(T6) alloy.

Fig. 11 depicts strain dependence of 2-D and 3-D *number* fraction of cracked Fe-rich intermetallic particles in the bulk microstructure of 5086(O) Al-alloy under a uniaxial compression. As expected, the number fraction of cracked particles (in both 2-D and 3-D) monotonically increases with an increase in the compressive strain. However, at any given strain, the 3-D number fraction of cracked particles is *higher* than the corresponding 2-D number fraction in the plane containing the extrusion axis (which is also the loading direction). A similar trend has been also observed in the 6061(T6) alloy [10]. Therefore, for deformation in compression, the 2-D number fraction of cracked particles significantly underestimates the 3-D number fraction of the cracked particles in the microstructural volume, which is the true damage parameter.

Fig. 12 compares the variation of 3-D number fraction of cracked Fe-rich intermetallic particles with applied true compressive stress in 5086 and 6061 Al-alloys, respectively. Recall that the yield stress of 5086(O) alloy is lower than that of 6061(T6) alloy. The extrapolated curve reveals that at stresses lower than the yield stress of 6061(T6) alloy, the damage is higher in 5086(O) alloy. This is consistent with the earlier observations [6] that plastic deformation of matrix is essential for particle cracking to occur. At any applied stress higher than the yields stress of both the alloys, the 3-D number fraction of cracked particles in 6061(T6) alloy is higher than its corresponding value for the 5086(O) alloy. Therefore, the 5086(O) alloy is less prone to the damage due to particle cracking compared to the 6061(O) alloy under a compressive load applied parallel to the extrusion axis. This may be due to lower volume fraction and lower average volume (and therefore, size)
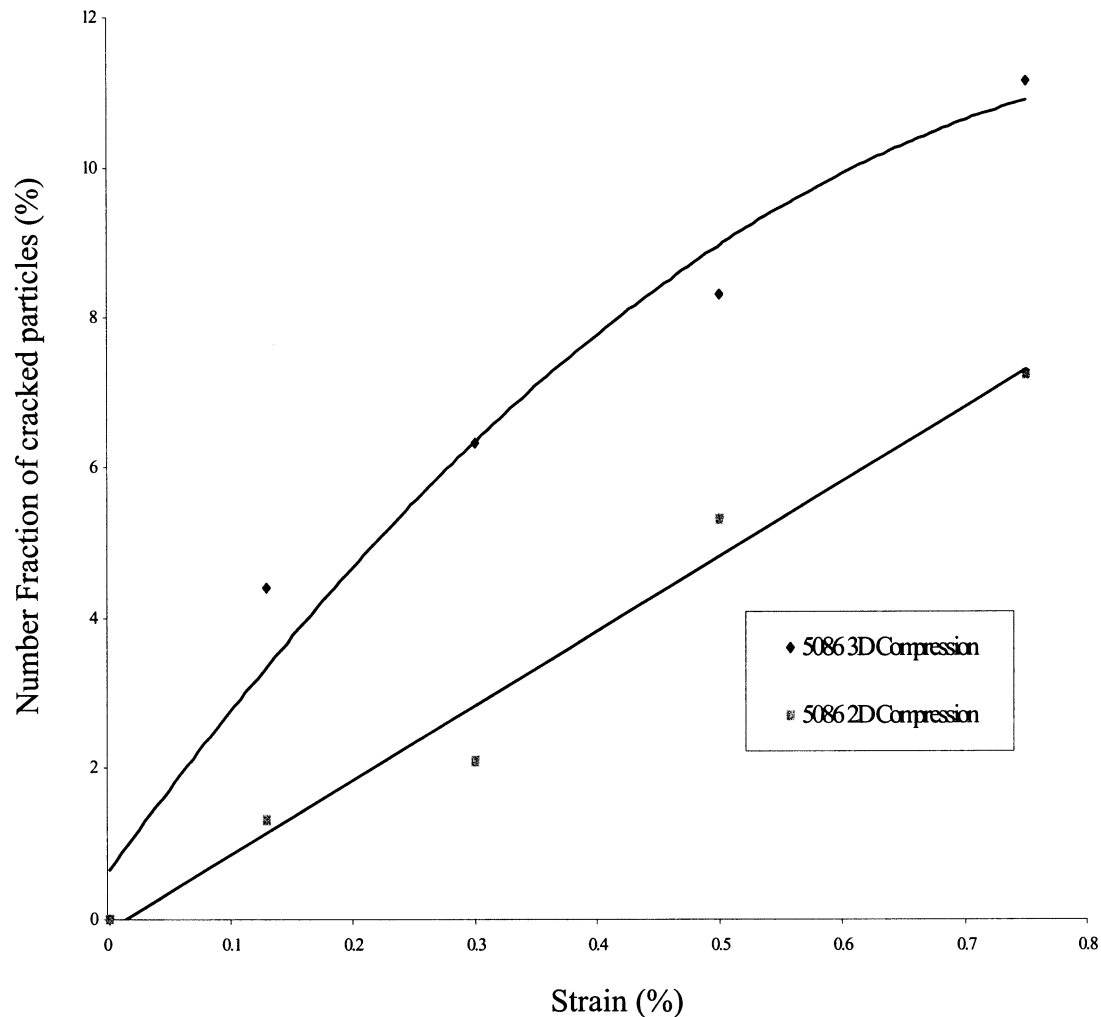
Fig. 11. Plot of number fraction of cracked Fe-rich particles in 2-D and 3-D versus compressive strain in 5086(O) alloy.

of the Fe-rich particles in the unstrained microstructure of the 5086(O) alloy (Table 2), differences in the chemical composition of the Fe-rich particles in the two alloys and the differences in the particle rotation tendencies in the two alloys. The higher extent of particle rotations in 6061(T6) alloy brings more particles in the orientations that facilitate particles cracking, thereby leading to a higher damage. These observations further demonstrate that the particle rotations and damage nucleation by particle cracking are inter-related. However, it must be pointed out that the additional factors, such as dynamic strain aging, may also affect the particle cracking damage evolution in the two alloys.

3.5. Particle cracking under uniaxial tension

Fig. 13 shows the variation of average cracked particle volume as a function of tensile strain in the 5086(O) and 6061(T6) alloys. Interestingly, unlike the variation observed in compression specimens (Fig. 9), the average volume of cracked Fe-rich particles in the

5086(O) alloy does *not* change significantly with tensile strain. The differences in the variation of averaged cracked particle volume with strain under compression and tension in the 5086(O) alloy are essentially due to the differences in the particle rotation tendency under these two loading conditions, when the load is applied parallel to the extrusion axis of the specimens. Significant rotations of Fe-rich particles do not occur, when a tensile load is applied parallel to the extrusion axis [24]. These observations are consistent with the hypothesis that the Fe-rich particles rotate and tend to align themselves along the direction of applied/induced tensile stress. In the unstrained specimens, most of the Fe-rich particles are aligned along the extrusion axis. Therefore, no significant particle rotations occur when the applied tensile stress direction is parallel to the extrusion axis. Under the tensile loading condition, the large particles that are almost parallel to the tensile loading direction are the first to crack. In the absence of significant particle rotations, as the tensile stress increases, additional particle cracking may occur due to cracking of
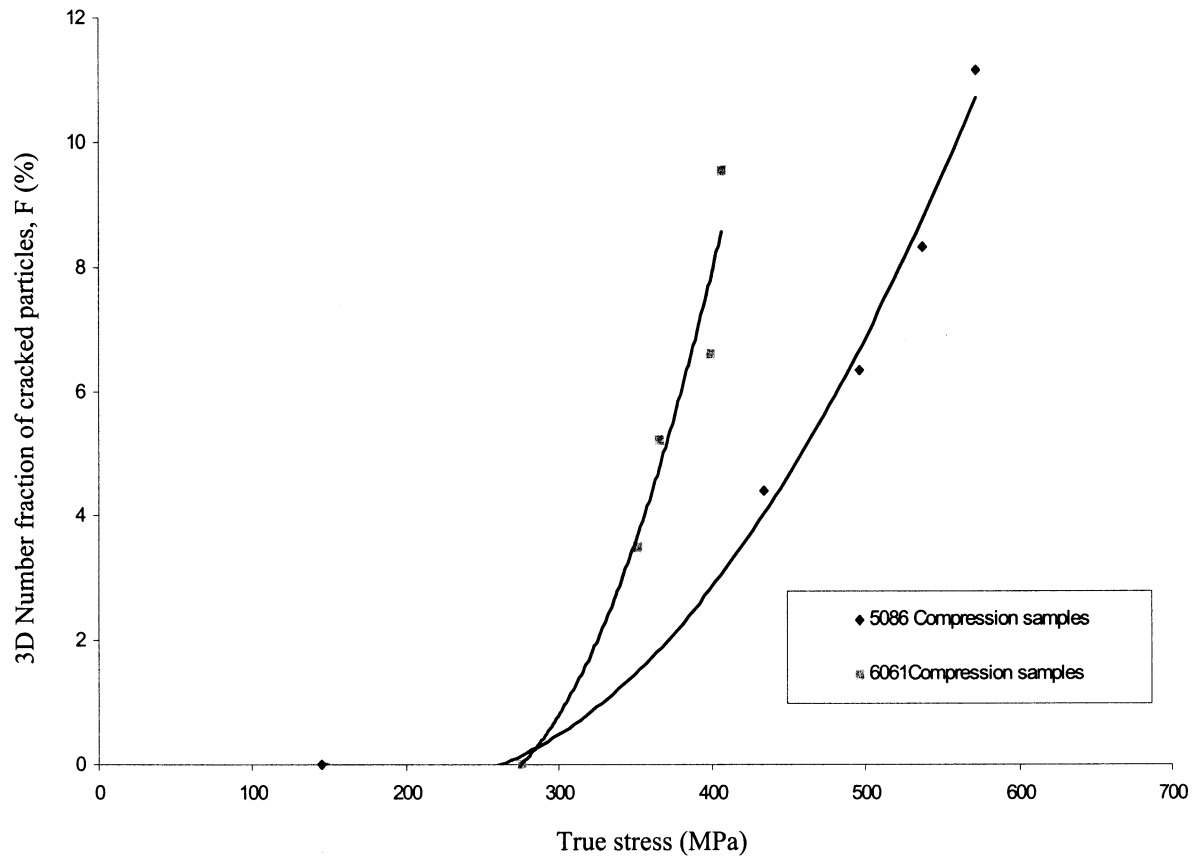
Fig. 12. Comparison of variation of 3-D number fraction of cracked Fe-rich particles with compressive strain in 6061(T6) and 5086(O) alloys.
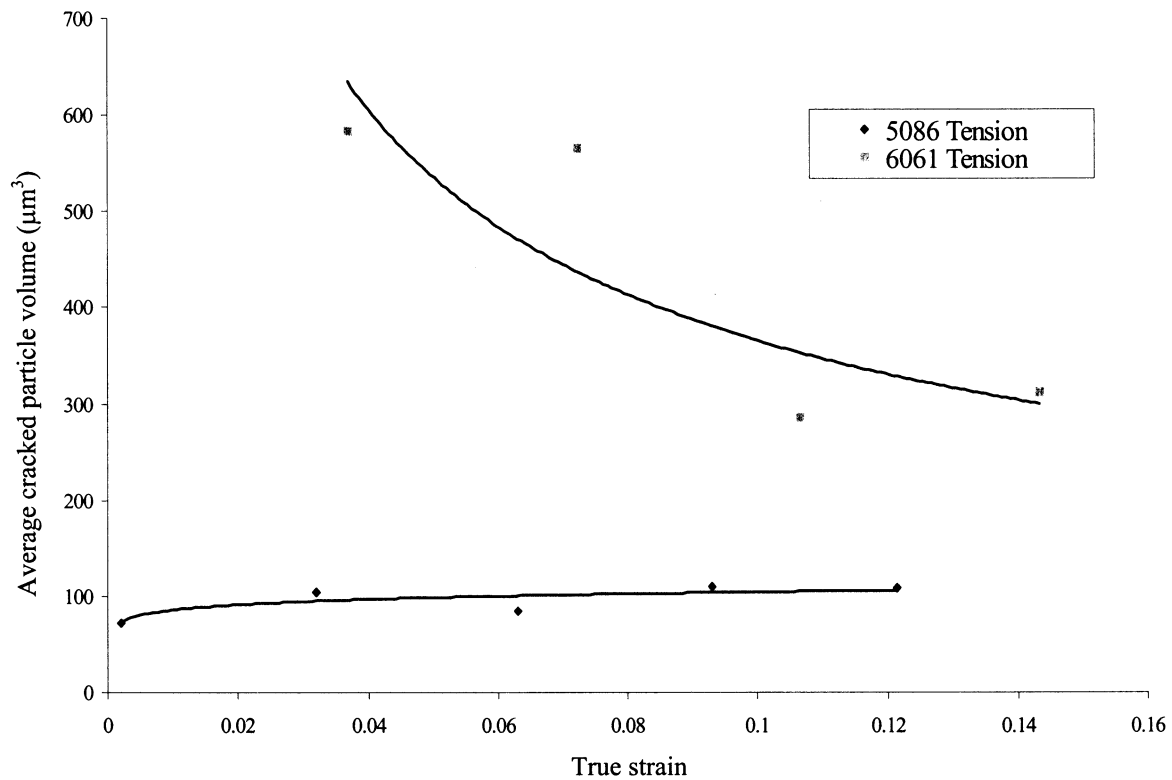

Fig. 13. Variation of average cracked particle volume as a function of tensile strain in the 5086(O) and 6061(T6) alloys.

smaller favorably oriented particles, or cracking of large particles that are not favorably oriented, or both. If additional particle cracking is predominantly due to cracking of progressively smaller favorably oriented particles with the increase in the tensile stress, then average cracked particle volume should decrease with an increase in the strain/stress, which is the trend observed in the 6061(T6) alloy [10,11]. On the other hand, if the additional particle cracking is predominantly due to cracking of large *unfavorably* oriented particles (having the sizes in the same regime as those cracked at lower strains), then the average cracked particle volume is not expected to change significantly with the tensile strain, which is the trend observed in the 5086(O) alloy. This is further supported by the data on morphological orientation distribution of cracked Fe-rich particles in the 5086(O) alloy shown in Fig. 14. At the tensile strain level of 0.0325, only 3% of cracked particles have the orientation angles larger than 40°, whereas at the tensile strain level of 0.129, >15% of the particles have orientation angles larger than 40°, which indicates that particles in unfavorable orientations (>40°) progressively crack with an increase in the tensile stress/strain. Therefore, it can be concluded that in 5086(O) alloy, when a tensile load is applied parallel to the extrusion axis, the progression of damage nucleation due to particle cracking is predominantly due to progressive cracking of large unfavorably oriented particles with an increase in the tensile stress/strain. On the other hand, in 6061(T6) alloy, when a tensile load is applied parallel to the extrusion axis, the progression of damage nucleation due to particle cracking is predominantly due to progressive cracking of *smaller* particles with an increase in the applied stress/strain.

Fig. 15 compares the variation of 3-D number fraction of cracked Fe-rich intermetallic particles with applied true tensile stress in 5086 and 6061 Al-alloys. At any applied tensile stress higher than the yields stress of both alloys, the 3-D number fraction of cracked particles in 6061(T6) alloy is higher than its corresponding value for the 5086(O) alloy. This trend is similar to the one observed under compressive loading parallel to the extrusion axis. Therefore, under both tensile and compressive loading parallel to the extrusion axis, the 5086(O) alloy is less prone to the particle cracking damage compared to the 6061(T6) alloy. This is likely to be due to number of different reasons including lower average size and volume fraction of Fe-rich particles in the unstrained microstructure of 5086(O) alloy; differences in the chemistry of the Fe-rich particles in the two
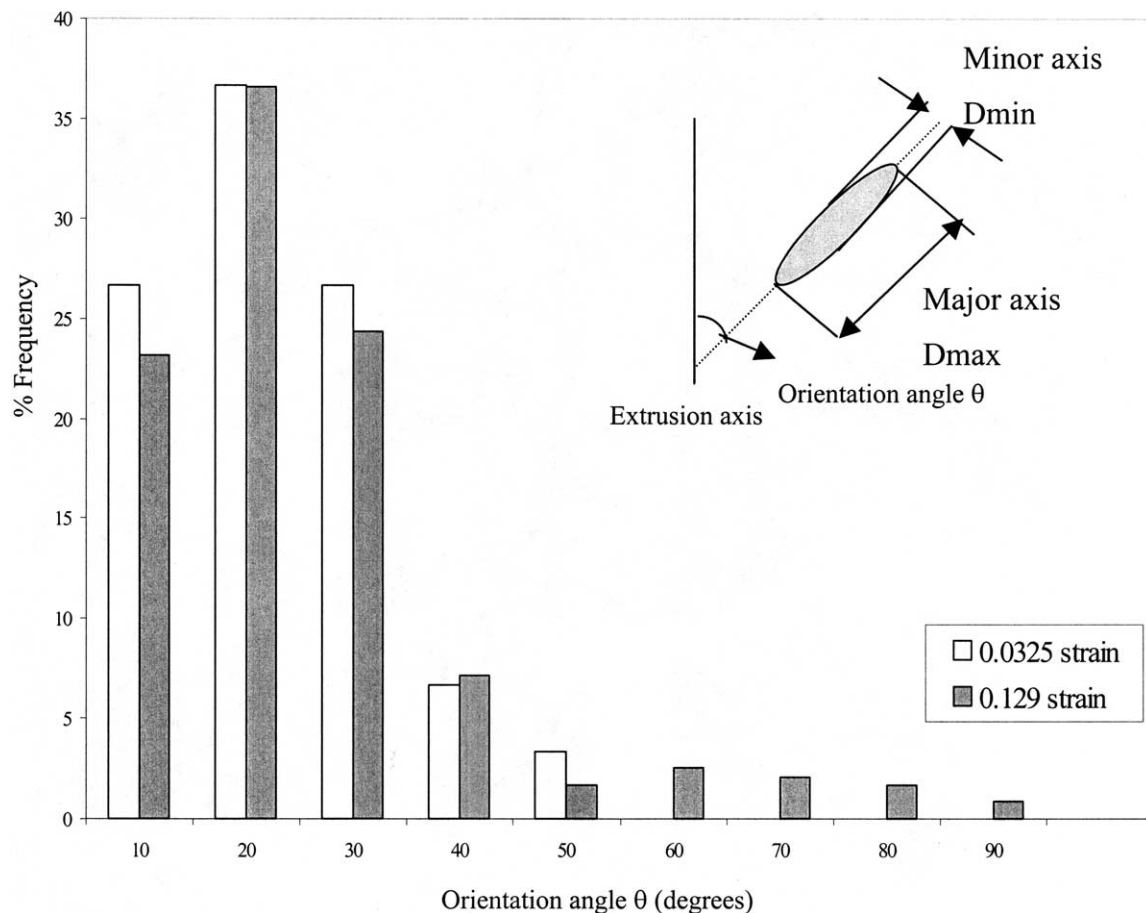

Fig. 14. Morphological orientation distribution of cracked Fe-rich particles in the 5086(O) alloy.
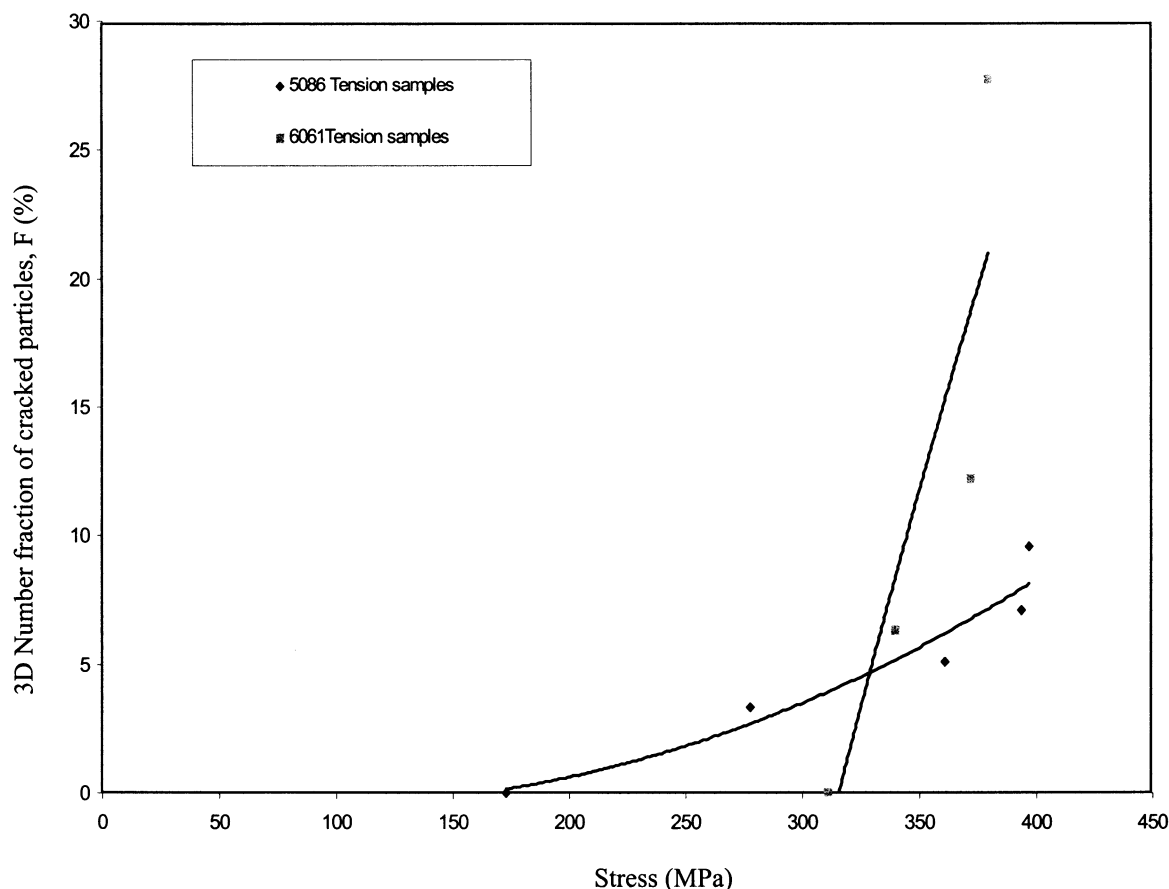
Fig. 15. Variation of 3-D number fraction of cracked Fe-rich intermetallic particles with applied true tensile stress in 5086 and 6061 Al-alloys.

alloys; lower particle rotation tendency in the 5086(O) alloy; and presence of DSA in the 5086(O) alloy. Further research is required to deconvolute the effects of the each of these factors on particle cracking.

4. Summary and conclusions

Stereology and image analysis have been used to quantify cracking of Fe-rich intermetallic particles in the 3-D microstructure of 5086(O) alloy. An analysis of these quantitative data and their comparison with the earlier data on 6061(T6) alloy leads to the following observations and conclusions.

In the 5086(O) alloy, cracking of Fe-rich intermetallic particles is the dominant damage nucleation mode. The cracks in the Fe-rich particles are mostly perpendicular to the direction of the major axis of the corresponding cracked particles. Therefore, particle cracking is strongly influenced by the local maximum principal stretch. The anisotropy of crack orientations strongly depends on the loading condition and stress state: under uniaxial tension, the cracks are mostly perpendicular to direction of applied load, whereas they are mostly

parallel to the loading direction when a compressive load is applied.

In both extruded alloys, the Fe-rich particles rotate during deformation under uniaxial compressive stress parallel to the extrusion axis and tend to align themselves along the direction of induced tensile stretch. These particle rotations in turn affect the progression of damage due to particle cracking. The extent of particle rotations is significantly lower in 5086(O) Al-alloy than in 6061(T6) alloy.

For the deformation under compression, in both alloys, the average volume of cracked particles *increases* with the compressive strain. However, the rate of increase of average cracked particle volume is significantly higher in the 5086(O) alloy compared to that in 6061(T6) Al-alloy. Therefore, progression of damage evolution involves cracking of more *larger* particles in the 5086(O) alloy compared to those in the 6061(T6) alloy.

In the 5086(O) alloy, at all strain levels in tension and compression, the 2-D number fraction of cracked particles is lower than the corresponding 3-D number fraction. Therefore, the 2-D observations consistently underestimate the true 3-D damage due to particle cracking.

At all tensile/compressive stress levels higher than the yield stress of both alloys, the 3-D number fraction of cracked particles in 5086(O) alloy is significantly *lower* than the corresponding value in the 6061(T6) alloy. Therefore, 5086(O) alloy is less prone to particle cracking damage than the 6061(T6) alloy.

Acknowledgements

References

[1] M.F. Horstemeyer, A.M. Gokhale, Int. J. Sol. Struct. 36 (1999) 5029.
[2] M.F. Horstemeyer, J. Lathrop, A.M. Gokhale, M. Dighe, Theor. Appl. Fract. Mech. 33 (2000) 31.
[3] A.F. McClintock, ASME J. Appl. Mech. 35 (1968) 363.
[4] A.L. Gurson, in: D.M.R. Taplin (Ed.), Proceedings of the International Conference on Fracture, vol. 2A, 1977, p. 357.
[5] E.E. Underwood, Quantitative Stereology, Addison-Wesley, Reading, MA, 1970.
[6] J.-W. Yeh, W.-P. Liu, Metall. Trans. 27A (1996) 3558.
[7] R. Doglione, J.L. Douziech, C. Berdin, D. Francois, Mater. Sci. For. (1996) 130.
[8] E.N. Pan, C.S. Lin, C.R. Loper, Am. Foundrym. Soc. Trans. 98 (1990) 735.
[9] J. Gurland, J. Plateau, Trans. ASM 56 (1963) 442.
[10] H. Agarwal, M.S. Thesis Dissertation, Georgia Institute of Technology, 2001.
[11] H. Agarwal, A.M. Gokhale, S. Graham, M.F. Horstemeyer, Metall. Mater. Trans. 33A (2002) 2599–2606.
[12] M. Wagenhofer, M. Erickson, R.W. Armstrong, F.J. Zerilli, Scr. Mater. 41 (1999) 1177.
[13] P. Louis, A.M. Gokhale, Metall. Mater. Trans. 26A (1995) 1449.
[14] H.B. Mcshane, C.P. Lee, T. Sheppard, Mater. Sci. Technol. 6 (1990) 428.
[15] D.C. Sterio, J. Microsc. 134 (1984) 127.
[16] A. Tewari, A.M. Gokhale, J. Microsc. 200 (2000) 227.
[17] A. Tewari, A.M. Gokhale, R.M. German, Acta Mater. 47 (1999) 3721.
[18] J. Polmear, Light Alloys: Metallurgy of Light Alloys, Halsted Press, New York, 1996, p. 67.
[19] J.M. Robinson, M.P. Shaw, Internat. Mater. Rev. 39 (1994) 113.
[20] G.E. Dieter, Mechanical Metallurgy, McGraw-Hill, New York, 1988, p. 197.
[21] K.L. Murthy, C.S. Seok, J. Metal. 53 (2001) 23.
[22] H. Agarwal, A.M. Gokhale, S. Graham, M.F. Horstemeyer, Mater. Sci. Eng. A328 (2002) 310.
[23] H. Agarwal, A.M. Gokhale, S. Graham, M.F. Horstemeyer, D.J. Bamann, Mater. Sci. Eng. A328 (2002) 310–316.
[24] A. Balasundaram, M.S. Dissertation, Georgia Institute of Technology, 2002.